Transport and optics at the node in a nodal loop semimetal

S. P. Mukherjee[1] and J. P. Carbotte[1,2]
[1]*Department of Physics and Astronomy, McMaster University, Hamiltion, Ontario, Canada L8S 4M1*
[2]*Canadian Institute for Advanced Research, Toronto, Ontario, Canada M5G 1Z8*
(Received 26 January 2017; revised manuscript received 17 May 2017; published 9 June 2017)

We use a Kubo formalism to calculate both AC conductivity and DC transport properties of a dirty nodal loop semimetal. The optical conductivity as a function of photon energy Ω exhibits an extended flat background $\sigma^{\rm BG}$ as in graphene provided the scattering rate Γ is small as compared to the radius of the nodal ring b (in energy units). Modifications to the constant background arise for $\Omega \leqslant \Gamma$ and the minimum DC conductivity $\sigma^{\rm DC}$, which is approached as Ω^2/Γ^2 as $\Omega \to 0$, is found to be proportional to $\frac{\sqrt{\Gamma^2+b^2}}{v_F}$ with v_F the Fermi velocity. For $b = 0$ we recover the known three-dimensional point node Dirac result $\sigma^{\rm DC} \sim \frac{\Gamma}{v_F}$ while for $b > \Gamma$, $\sigma^{\rm DC}$ becomes independent of Γ (universal) and the ratio $\frac{\sigma^{\rm DC}}{\sigma^{\rm BG}} = \frac{8}{\pi^2}$ where all reference to material parameters has dropped out. As b is reduced and becomes of the order Γ, the flat background is lost as the optical response evolves towards that of a three-dimensional point node Dirac semimetal which is linear in Ω for the clean limit. For finite Γ there are modifications from linearity in the photon region $\Omega \leqslant \Gamma$. When the chemical potential μ (temperature T) is nonzero the DC conductivity increases as $\mu^2/\Gamma^2(T^2/\Gamma^2)$ for $\frac{\mu}{\Gamma}$ $(\frac{T}{\Gamma}) \leqslant 1$. Such laws apply as well for thermal conductivity and thermopower with coefficients of the quadratic law only slightly modified from their value in the three-dimensional point node Dirac case. However in the $\mu = T = 0$ limit both have the same proportionality factor of $\sqrt{\Gamma^2+b^2}$ as does $\sigma^{\rm DC}$. Consequently the Lorentz number is largely unmodified. For larger values of $\mu > \Gamma$ away from the nodal region the conductivity shows a Drude-like contribution about $\Omega \approxeq 0$ which is followed by a dip in the Pauli blocked region $\Omega \leqslant 2\mu$ after which it increases to merge with the flat background (two-dimensional graphene like) for $\mu < b$ and to the quasilinear (three-dimensional point node Dirac) law for $\mu > b$.

DOI: 10.1103/PhysRevB.95.214203

I. INTRODUCTION

Optical (IR) along with other spectroscopies such as angular resolved photoemission ARPES and scanning tunnelling microscopy have given us a wealth of information on the dynamics of charge carriers in metals and superconductors [1–3] with different gap symmetries. More recently the dynamic optical conductivity $\sigma(T,\Omega)$ as a function of temperature and photon energy has been equally successful when applied to the class of two-dimensional (2D) metals such as graphene [4–6], the surface states of topological insulators [7,8], as well as topological materials such as Dirac and Weyl semimetals [9–17].

Another recent development has been the discovery of nodal loop semimetals [18–28]. Their magnetic susceptibility [29], density fluctuation plasmons and Friedel oscillations [30], Landau quantization [31], some aspect of their topological electrodynamic response [32], and correlation effects [33] have been studied. The dynamical optical conductivity as a function of photon energy Ω has also been considered in the clean limit [34]. It was found to display signatures of both three-dimensional (3D) point node Weyl or Dirac-like materials and 2D graphene-like systems, depending on what range of photon energy Ω is used to probe the dynamics. For Ω small compared with twice the radius in energy units of the nodal ring (b), the response is 2D in nature while for $\Omega > 2b$ it evolves to 3D, characteristic of point node Dirac. In any realistic case, the charge carriers will also have a finite scattering rate Γ which influences their motion. In this paper we study the effect of Γ on the electromagnetic properties of a nodal loop semimetal at finite chemical potential and photon energy. In addition, we consider DC transport including conductivity, thermal conductivity, thermopower, and Lorentz number. Here we will be particularly but not exclusively interested in the case when the chemical potential μ and temperature T are small compared with Γ which allows optics and transport at the nodes to be probed. This regime includes the concept of minimum conductivity and how it is modified when μ and/or T is increased out of zero.

In Sec. II we present the necessary formalism including the Kubo formula for the dynamical conductivity $\sigma(T,\Omega)$ at finite T and photon energy. Results at finite photon energy are given in Sec. III. While many of our results are for $\mu = 0$ (nodal region) the effect of a finite chemical potential are also presented. In Sec. IV we consider DC properties, electrical conductivity, thermal conductivity, thermopower, and Lorentz number. A discussion and conclusion can be found in Sec. V.

II. FORMALISM

The continuum 4×4 matrix Hamiltonian for a loop node semimetal on which our work is based takes the form

$$\hat{H} = v_F \hat{\tau}_x(\hat{\sigma}.\mathbf{p}) + b\hat{\tau}_z\hat{\sigma}_x, \tag{1}$$

where v_F is the Fermi velocity, $\mathbf{p}$ is the momentum equal to $\mathbf{k}$, and b is a Zeeman field oriented along the x axis. The 2×2 matrix $\hat{\tau}$ and $\hat{\sigma}$ are each a set of Pauli matrices. For convenience in our calculation we will set $v_F = \hbar = 1$ and only at the end restore them. The energies of the two sets of bands involved can be written as

$$\epsilon_{ss'}(\mathbf{k}) = s\sqrt{k_x^2 + \left(\sqrt{k_y^2+k_z^2} + s'b\right)^2} = s\epsilon_{s'}(\mathbf{k}), \tag{2}$$

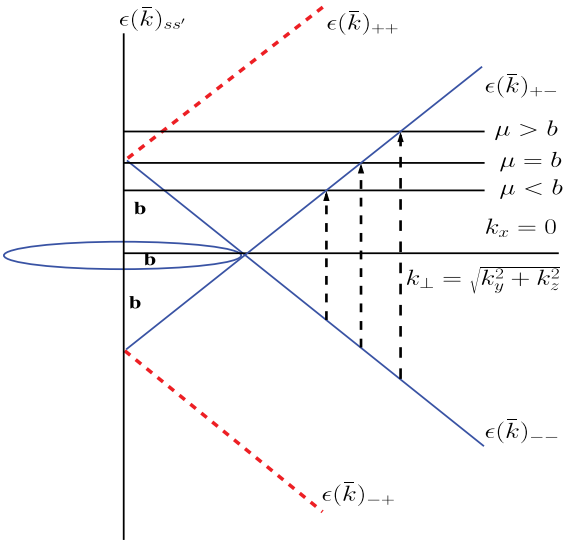

FIG. 1. Schematic diagram showing the electron dispersion curves $\epsilon_{ss'}(\mathbf{k}) = s\sqrt{k_x^2 + (\sqrt{k_y^2 + k_z^2} + s'b)^2}$. In the figure $k_x = 0$ and $k_\perp = \sqrt{k_y^2 + k_z^2}$. $\epsilon_{+s'}(\mathbf{k})$ represents the conduction band and $\epsilon_{-s'}(\mathbf{k})$ the valence band. There are two branches $s' = +1$ (dashed red curve) which has no nodes and $s' = -1$ (dashed blue curve) which involves a nodal circle depicted as the solid blue circle of radius b. The vertical arrows show the minimum interband optical transitions possible for the three values of the chemical potential μ shown $\mu < b$, $\mu = b$, and $\mu > b$. Transitions with shorter arrows are Pauli blocked and hence are not possible.

where $s' = \pm$ and $s = \pm$. The index s gives conduction $(+1)$ and valence (-1) band associated with the dispersion curves of the s' band. These dispersion curves are highlighted in Fig. 1.

The zz component of the dynamical conductivity $\sigma_{zz}(\Omega)$ which can be calculated from the Kubo formula depends on the spectral density $A_{ss'}(\omega)$ of the charge carriers and takes the form

$$\sigma_{zz}^{\rm IB}(\Omega) = \frac{e^2\pi}{\Omega}\int_{-\infty}^{+\infty} d\omega[f(\omega) - f(\omega+\Omega)]\sum_{ss'}\int\frac{d^3\mathbf{k}}{(2\pi)^3} \times\left(1 - \frac{k_x^2}{\epsilon_{ss'}^2(\mathbf{k})}\right)A_{ss'}(\mathbf{k},\omega)A_{-ss'}(\mathbf{k},\omega+\Omega), \quad (3)$$

for the interband transitions $[\sigma_{zz}^{\rm IB}(\Omega)]$ and the intraband part $[\sigma_{zz}^{D}(\Omega)]$ is given by the formula

$$\sigma_{zz}^{D}(\Omega) = \frac{e^2\pi}{\Omega}\int_{-\infty}^{+\infty} d\omega[f(\omega) - f(\omega+\Omega)]\sum_{ss'}\int\frac{d^3\mathbf{k}}{(2\pi)^3} \times\frac{k_x^2}{\epsilon_{ss'}^2(\mathbf{k})}A_{ss'}(\mathbf{k},\omega)A_{ss'}(\mathbf{k},\omega+\Omega). \quad (4)$$

In terms of the carrier self energy $\Sigma_{ss'}(\omega)$, the spectral functions take the form [6]

$$A_{ss'}(\mathbf{k},\omega) = \frac{1}{\pi}\frac{|-\Im\Sigma_{ss'}(\omega)|}{(\omega - \Re\Sigma_{ss'}(\omega) - \epsilon_{ss'}(\mathbf{k}))^2 + (\Im\Sigma_{ss'}(\omega))^2}. \quad (5)$$

For simplicity in our calculation we will take the case of residual scattering modeled through a constant imaginary part $|-\Im\Sigma_{ss'}(\omega)| \equiv \Gamma$. We will consider two limiting cases for Eq. (3). The DC limit of $\Omega \to 0$ in which instance the thermal factor

$$\lim_{\Omega\to 0}\left\{\frac{f(\omega) - f(\omega+\Omega)}{\Omega}\right\} = -\frac{\partial f(\omega)}{\partial\omega}, \quad (6)$$

where $f(\omega)$ is the Fermi-Dirac thermal distribution function. The zero temperature case for which the integral over ω becomes limited to the range μ to $\mu - \Omega$ where μ is the chemical potential and the thermal factor $[f(\omega) - f(\omega+\Omega)]$ is to be replaced by 1.

The $T = 0$ limit involves an integral over ω of the form

$$\int_{\mu-\Omega}^{\mu}\frac{d\omega}{\pi^2}\frac{\Gamma}{(\omega - \epsilon_{ss'}(\mathbf{k}))^2 + \Gamma^2} \times \frac{\Gamma}{(\omega + \Omega - \epsilon_{ss'}(\mathbf{k}))^2 + \Gamma^2}, \quad (7)$$

which can be done analytically and gives

$$\frac{\sigma_{zz}^{\rm IB}(T=0,\Omega)}{\Gamma} = \frac{e^2}{2\pi^3\hbar^2 v_F}\sum_{s'}\int_0^\infty\frac{d\widetilde{k}_x}{\widetilde{\Omega}}\int_0^\infty\widetilde{\rho}d\widetilde{\rho} \times\left(1 - \frac{\widetilde{k}_x^2}{\widetilde{\epsilon}_{s'}^2}\right)\mathfrak{Y}(\widetilde{\mu},\widetilde{\Omega},\widetilde{b},\widetilde{\epsilon}_{s'}), \quad (8)$$

where we have introduced polar coordinates for k_y, k_z variables and have divided all variables by the scattering rate which has had the effect of scaling out Γ. Of course it remains in $\widetilde{\Omega} \equiv \frac{\Omega}{\Gamma}, \widetilde{\mu} \equiv \frac{\mu}{\Gamma}$ and $\widetilde{b} \equiv \frac{b}{\Gamma}$ while the other variables are dummies of integration. The function $\mathfrak{Y}(\widetilde{\mu},\widetilde{\Omega},\widetilde{b},\widetilde{\epsilon}_{s'})$ has the form

$$\mathfrak{Y}(\widetilde{\mu},\widetilde{\Omega},\widetilde{b},\widetilde{\epsilon}_{s'}) = \frac{1}{(\widetilde{\Omega} + 2\widetilde{\epsilon}_{s'})[4 + (\widetilde{\Omega} + 2\widetilde{\epsilon}_{s'})^2]}\Bigg[\ln\left(\frac{1 + (\widetilde{\mu} + \widetilde{\Omega} + \widetilde{\epsilon}_{s'})^2}{1 + (\widetilde{\mu} - \widetilde{\epsilon}_{s'})^2} \times \frac{1 + (\widetilde{\mu} - \widetilde{\Omega} - \widetilde{\epsilon}_{s'})^2}{1 + (\widetilde{\mu} + \widetilde{\epsilon}_{s'})^2}\right) + (\widetilde{\Omega} + 2\widetilde{\epsilon}_{s'})\{\arctan(\widetilde{\mu} + \widetilde{\Omega} + \widetilde{\epsilon}_{s'}) + \arctan(\widetilde{\mu} - \widetilde{\epsilon}_{s'}) - \arctan(\widetilde{\mu} + \widetilde{\epsilon}_{s'}) - \arctan(\widetilde{\mu} - \widetilde{\Omega} - \widetilde{\epsilon}_{s'})\}\Bigg] + \frac{1}{(\widetilde{\Omega} - 2\widetilde{\epsilon}_{s'})[4 + (\widetilde{\Omega} - 2\widetilde{\epsilon}_{s'})^2]}\Bigg[\ln\left(\frac{1 + (\widetilde{\mu} + \widetilde{\Omega} - \widetilde{\epsilon}_{s'})^2}{1 + (\widetilde{\mu} + \widetilde{\epsilon}_{s'})^2} \times \frac{1 + (\widetilde{\mu} - \widetilde{\Omega} + \widetilde{\epsilon}_{s'})^2}{1 + (\widetilde{\mu} - \widetilde{\epsilon}_{s'})^2}\right) + (\widetilde{\Omega} - 2\widetilde{\epsilon}_{s'})\{\arctan(\widetilde{\mu} + \widetilde{\Omega} - \widetilde{\epsilon}_{s'}) + \arctan(\widetilde{\mu} + \widetilde{\epsilon}_{s'}) - \arctan(\widetilde{\mu} - \widetilde{\epsilon}_{s'}) - \arctan(\widetilde{\mu} - \widetilde{\Omega} + \widetilde{\epsilon}_{s'})\}\Bigg]. \quad (9)$$

An equivalent equation can be derived for the intraband case. We obtain

$$\frac{\sigma^{D}_{zz}(T=0,\Omega)}{\Gamma} = \frac{e^2}{2\pi^3\hbar^2 v_F}\sum_{s'}\int_0^\infty \frac{d\widetilde{k}_x}{\widetilde{\Omega}}\int_0^\infty \widetilde{\rho}\,d\widetilde{\rho}\,\frac{\widetilde{k}_x^2}{\widetilde{\epsilon}_{s'}^2}\,\mathfrak{H}(\widetilde{\mu},\widetilde{\Omega},\widetilde{b},\widetilde{\epsilon}_{s'}), \tag{10}$$

with

$$\mathfrak{H}(\widetilde{\mu},\widetilde{\Omega},\widetilde{b},\widetilde{\epsilon}_{s'}) = \frac{1}{\widetilde{\Omega}[\widetilde{\Omega}^2+4]}\Bigg[\ln\left(\frac{(1+(\widetilde{\mu}+\widetilde{\Omega}+\widetilde{\epsilon}_{s'})^2)}{1+(\widetilde{\mu}+\widetilde{\epsilon}_{s'})^2}\frac{(1+(\widetilde{\mu}+\widetilde{\Omega}-\widetilde{\epsilon}_{s'})^2)}{1+(\widetilde{\mu}+\widetilde{\epsilon}_{s'})^2}\frac{(1+(\widetilde{\mu}-\widetilde{\Omega}+\widetilde{\epsilon}_{s'})^2)}{1+(\widetilde{\mu}-\widetilde{\epsilon}_{s'})^2}\frac{(1+(\widetilde{\mu}-\widetilde{\Omega}-\widetilde{\epsilon}_{s'})^2)}{1+(\widetilde{\mu}-\widetilde{\epsilon}_{s'})^2}\right)$$
$$+\widetilde{\Omega}\{\arctan(\widetilde{\mu}+\widetilde{\Omega}+\widetilde{\epsilon}_{s'})+\arctan(\widetilde{\mu}+\widetilde{\Omega}-\widetilde{\epsilon}_{s'})-\arctan(\widetilde{\mu}-\widetilde{\Omega}+\widetilde{\epsilon}_{s'})-\arctan(\widetilde{\mu}-\widetilde{\Omega}-\widetilde{\epsilon}_{s'})\}\Bigg]. \tag{11}$$

We have checked that these equations properly reduce to the clean limit forms for $\Gamma \to 0$ used in the work of Ref. [34] with which we will compare when appropriate.

III. RESULTS FOR FINITE FREQUENCIES

In Fig. 2 we show our results for the zero temperature dynamic optical response $\sigma(T=0,\Omega)$ as a function of photon energy Ω both quantities normalized by the optical scattering rate Γ, i.e., $\sigma(T=0,\Omega)/\Gamma$ vs Ω/Γ. In these reduced variables Γ has dropped out and we have a single set of curves which apply for any value of Γ. In fact we have a family of curves defined by two external parameters, the normalized chemical potential $\mu/\Gamma \equiv \widetilde{\mu}$ and nodal loop parameter $b/\Gamma \equiv \widetilde{b}$. Here $\widetilde{\mu}=0$ represents charge neutrality and we consider nine values of b/Γ. Starting from the top curve we see a graphene-like 2D constant background extending from a bit above of $\Omega=0$ all the way to $\Omega=2b$ at which point it shows a transition to a linear in Ω/Γ behavior characteristic of a 3D point node Dirac material. The height of this plateau referred to as the interband background [35] and denoted by σ^{BG} agrees (after a correction of a dropped factor of 2) with the value obtained in Ref. [34] where the clean limit $\Gamma \to 0$ was considered. At $\Omega/\Gamma \to 0$ however our new results show a bend downward to connect with the DC value of the conductivity as we will discuss shortly. As the value of the nodal loop parameter is reduced towards zero the frequency range over which a plateau is well defined shrinks. It is still seen in the dashed blue curve for $b/\Gamma=6$ but below this value we see a clear evolution from a constant value to linear-like behavior characteristic of a 3D Dirac point node system as we will elaborate upon in Fig. 4. First we return to the $\Omega=0$ limit. As we will see later [Eq. (20)] we get a particularly simple and important result

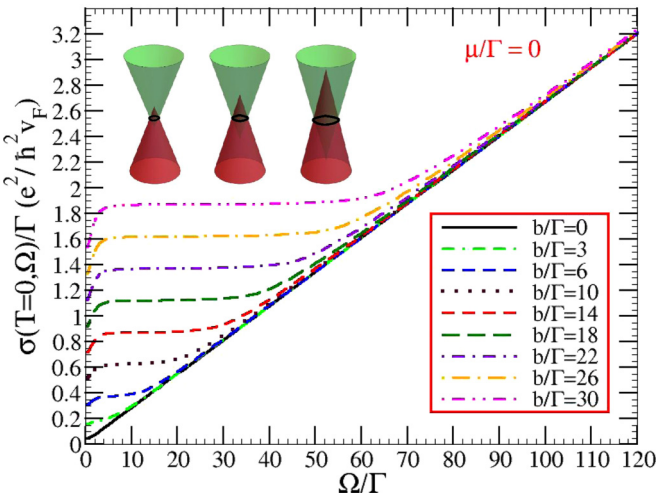

FIG. 2. The conductivity $\sigma(T=0,\Omega)$ normalized by the scattering rate Γ in units of $\frac{e^2}{\hbar^2 v_F}$ as a function of normalized photon energy Ω/Γ. Various values of b/Γ are shown with b the loop node radius in energy units. The chemical potential μ is set equal to zero. Except for the smaller values of b/Γ the 2D graphene-like constant background conductivity is well developed for photon energies Ω below $2b$. For photon energies above $2b$ the linear law of the 3D Dirac point node case is recovered. At small values of Ω there is a downturn of the constant background to its minimum DC value at $\Omega=0$.

$$\sigma^{DC} = \frac{e^2}{\hbar^2 v_F}\frac{1}{2\pi^2}\sqrt{\Gamma^2+b^2}. \tag{12}$$

In the limit $b=0$ which here corresponds to a 3D point node Dirac model we get the known answer obtained in Ref. [16], namely the minimum conductivity σ^{DC} is not universal but rather depends linearly on optical scattering rate (twice the quasiparticle rate Γ). This is a very different result from that obtained for graphene [6] for which σ^{DC} is simply a number $\frac{4e^2}{\pi h}$ in the same constant Γ approximation used here and referred to as the universal interband background (σ^{BG}). We see however from Eq. (12) that in the nodal loop semimetal Γ drops out of σ^{DC} if $b \gg \Gamma$ and in that case we get no dependence on scattering rate Γ so σ^{DC} is again universal equal to $\frac{e^2}{\hbar^2 v_F}\frac{b}{2\pi^2}$. While this minimum conductivity does not depend on Γ it is linear in b and inversely dependent on v_F which are material dependent properties. In graphene no such material parameters arise [6]. A universal conductivity [36] is also part of d-wave [3] superconductivity theory. It arises when a gap which can have complex symmetry [37,38] nevertheless goes through a zero [39,40] on the Fermi surface. It does not arise in an s-wave superconductor even if there is some anisotropy such as in Al [41] but with no zero. We note that the magnitude of minimum conductivity depends on the model used for the disorder as discussed in the review of Evers and Mirlin [42] for the specific case of graphene and many other Refs. [43–45]. Here only the simplest model of constant scattering was used. This can be expected if the density of state at charge neutrality is finite as argued in Ref. [43].

The approach to the minimum DC conductivity and more generally the transition from 2D graphene-like behavior for the AC conductivity to 3D point node Dirac behavior as b gets small is further elaborated upon in Fig. 3. Again we

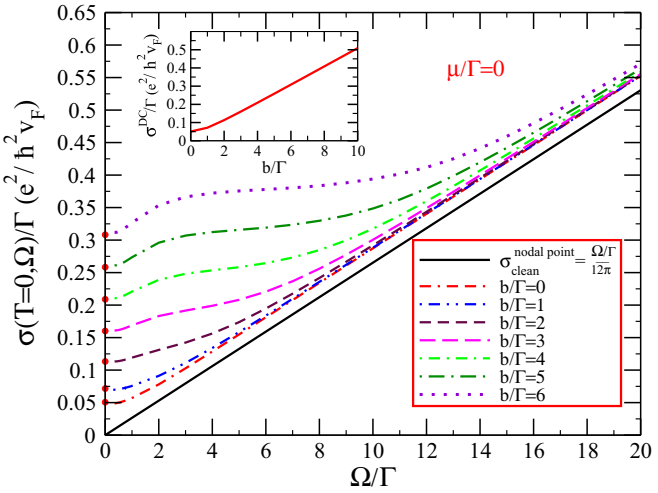

FIG. 3. The conductivity $\sigma(T=0,\Omega)$ normalized by the scattering rate Γ in units of $\frac{e^2}{\hbar^2 v_F}$ as a function of normalized photon energy Ω/Γ. We show the transition from a 2D graphene-like constant background for $\Omega < 2b$ (dotted violet curve) to the linear in Ω behavior of a 3D Dirac point node as b/Γ is reduced from a value of six to zero when the double-dashed-dotted red curve applies. This last curve still differs from the solid black curve which applies in the clean limit and is a straight line of slope $\frac{1}{12\pi}$ in our units. The DC limit of these curves $[\sigma^{\rm DC}(T=0,\mu=0)]$ is shown with heavy red points on the $\Omega/\Gamma=0$ axis and is never zero when some scattering is included. The inset shows how it evolves as a function of b/Γ.

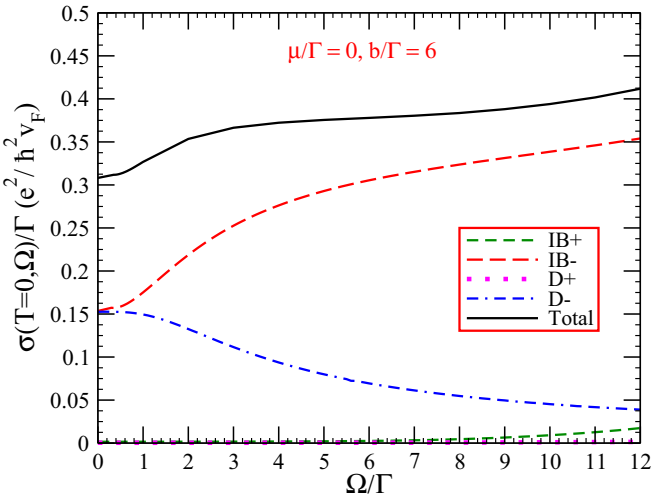

FIG. 4. The conductivity $\sigma(T=0,\Omega)$ normalized by the scattering rate Γ in units of $\frac{e^2}{\hbar^2 v_F}$ as a function of normalized photon energy Ω/Γ for the case $\mu/\Gamma=0$ and $b/\Gamma=6$ (solid black line). The other curves show the decomposition of the conductivity in terms of the intra- (D) and inter- (IB) band optical transitions and the two bands $s'=\pm$. The $s'=+1$ band is gapped by b and does not contribute much. The $s'=-1$ band in contrast shows that at $\Omega=0$ (DC limit) both intra- (Drude) and interband contributions are equal. As Ω/Γ is increased IB$_-$ increases while D$_-$ decreases as we expect.

show the photon energy dependence of the zero temperature conductivity $\sigma(T=0,\Omega)$ both normalized by Γ so as to get universal curves but here we consider only values of b less than $b/\Gamma=6$ (dotted violet curve). While this curve still shows a clear tendency to flatten out in the region around $\Omega/\Gamma\approx 5$, the other results do not. By $b/\Gamma=1$ the curve for $\sigma(T=0,\Omega)/\Gamma$ vs Ω/Γ is convex upward and no trace of a plateau remains. The dot-double-dashed red curve for $b=0$ reproduces the results of Ref. [16] for a 3D Dirac point node semimetal. We have also placed on the same graph their results (solid black curve) for the clean limit. A straight line of slope $\frac{1}{12\pi}$ applies in this case. In the inset to Fig. 3 we show the evolution of minimum DC conductivity $\sigma^{\rm DC}$ normalized to Γ as a function of b/Γ from Eq. (12), which in our units is $\frac{1}{2\pi^2}\sqrt{1+(b/\Gamma)^2}$. We see that it rapidly goes from a constant $\frac{1}{2\pi^2}$ to $\frac{b/\Gamma}{2\pi^2}$ linear in b and inversely proportional to Γ. These results are plotted on the $\Omega=0$ axis of the main frame as heavy red dots.

It is important to understand that when residual scattering (finite Γ) is introduced both interband and intraband optical transition contribute to the minimum conductivity Eq. (12) as they do to finite photon energy properties. This is illustrated in Fig. 4 where we treat the specific case $\mu/\Gamma=0$, $b/\Gamma=6$ for definiteness. We have decomposed the contributions to $\sigma(T=0,\Omega)$ into four terms. The dashed green line is the interband (IB) contribution of the $s'=+1$ band and the dashed red line is for $s'=-1$, the dotted magenta line is the intraband (D) contribution with $s'=+1$ and the double-dashed-dotted blue line for $s'=-1$. It is clear and expected that the $s'=+1$ band contributes little to the conductivity in the region $\Omega<2b$ because it is gapped as can be seen in Fig. 1. In fact if we had not included some scattering ($\Gamma=0$) these contributions would be identically zero in the clean limit. Even for $\Gamma\neq 0$ it is the $s'=-1$ that gives almost the entire contribution from interband (dashed red curve) and intraband (double-dashed-dotted blue curve) optical transitions. Note that at $\Omega=0$ (DC limit) both give exactly the same contribution. This is entirely due to the presence of finite Γ. In the clean limit there is no intraband conductivity because the chemical potential $\mu=0$ in our example and the entire DC conductivity comes from the interband transitions. Thus scattering has a profound effect on these results.

In Fig. 5 we elaborate further on the relationship of our results to the clean limit results of Refs. [16,34]. What is shown as the solid red curve is $\sigma(T=0,\Omega)$ normalized with Γ in units of $\frac{e^2}{\hbar^2 v_F}$ as a function of Ω/Γ for a case $\mu/\Gamma=2$ and $b/\Gamma=10$. In this example a Drude-like peak is clearly seen in the vicinity of $\Omega/\Gamma\approx 0$. This contribution would exist even in the clean limit but would take the form of a Dirac delta function at $\Omega=0$. For comparison with the clean limit we also show as a solid blue line the clean limit result of Ref. [34] corrected for a missing factor of 2. We have,

$$\frac{\sigma^{\rm IB}(\Omega)}{\Gamma}=\frac{e^2\pi}{\hbar^2 v_F}\frac{1}{2\Omega\Gamma}I\left(\frac{\Omega}{2}\right), \tag{13}$$

with

$$I(\omega)=\frac{\omega b}{4\pi} \quad \omega<b,$$
$$=\frac{1}{2\pi^2}\left[b|\omega|\arctan\frac{b}{\sqrt{\omega^2-b^2}}+\frac{\sqrt{\omega^2-b^2}}{3|\omega|}(4\omega^2-b^2)\right] \quad \omega>b. \tag{14}$$

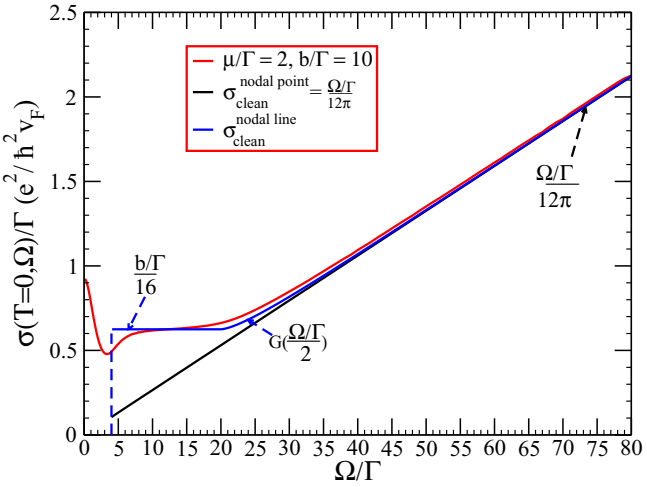

FIG. 5. The conductivity $\sigma(T=0,\Omega)$ normalized by the scattering rate Γ in units of $\frac{e^2}{\hbar^2 v_F}$ as a function of normalized photon energy Ω/Γ. A case of chemical potential $\mu/\Gamma = 2$ and $b/\Gamma = 10$ (solid red curve) is compared with the clean limit results obtained in Ref. [34] for a loop node semimetal (solid blue curve) as well as with the 3D Dirac point node model (solid black curve) in Ref. [16]. At the higher values of Ω shown all these curves merge and define a straight line of slope $\frac{1}{12\pi}$ in our units. This straight line continues in the point node case until $\Omega = 2\mu$ where it drops to zero. The lost optical spectral weight is transferred to a Dirac delta function at $\Omega = 0$ (not seen here). For the nodal loop there is a short region in photon energy where the straight line of slope $\frac{1}{12\pi}$ changes to a constant of height $\frac{b/\Gamma}{16}$ at $\Omega = 2b$ and is again cut off at $\Omega = 2\mu$. The solid red line is different but still shows a plateau-like region below $\Omega = 2b$ but there is no sharp cutoff at $\Omega = 2\mu$ for two reasons. First the optical weight transferred to the intraband transitions is now broaden into a Drude part of width 2Γ, and the interband background is also smeared out by the residual scattering.

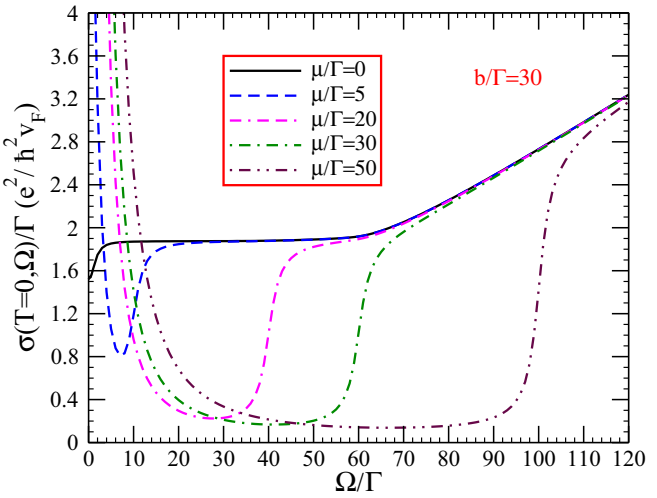

FIG. 6. The conductivity $\sigma(T=0,\Omega)$ normalized by the scattering rate Γ in units of $\frac{e^2}{\hbar^2 v_F}$ as a function of normalized photon energy Ω/Γ. In all cases b/Γ is set to be 30 while five different values of chemical potential are considered ranging from $\mu/\Gamma = 0$ to $\mu/\Gamma = 50$ which is almost twice the value of b/Γ chosen. Except for the $\mu/\Gamma = 0$ case (solid black line) the curves all show a Drude-like peak at small values of Ω/Γ. These peaks increase with the value of μ/Γ as a result of increasing optical spectral weight transfer from the interband to intraband optical transitions. When μ/Γ is small compared with b/Γ the 2D graphene-like constant background is recovered as Ω/Γ increases while for the last curve with $\mu > b$ the recovery is to the 3D Dirac point node linear in Ω law.

This is plotted as a blue solid line [labeled as $G(\frac{\Omega/\Gamma}{2})$] which is cut off below 2μ because interband optical transitions are not possible below this photon energy because of Pauli blocking (see Fig. 1). The optical spectral weight lost is of course transferred to a delta function at $\Omega = 0$ not shown on the figure. Having understood that at finite Γ this spectral weight is distributed into a Drude-like form around $\Omega = 0$ we see that the clean limit results agree very well with our new results for the finite Γ case (solid red curve). We have also placed for additional comparison the results of Ref. [16] for point node Dirac as a solid black curve which is a straight line of slope $\frac{1}{12\pi}$. It too is to be cut off at $\Omega = 2\mu$. While it matches well with the other two curves in the large Ω region it is very different from the nodal loop results below $\Omega = 2b$.

In Fig. 6 we present additional results for the case of finite chemical potential. Here b/Γ is fixed at 30, and five values of μ/Γ are considered. The solid black line is for $\mu = 0$ and has already been presented in Fig. 2 as a dashed-double-dotted magenta line. It is repeated here for comparison. The finite μ curves all show a large Drude-like peak at small photon energies. Beyond this Drude, all curves show a depression in conductivity before rising up again to meet the $\mu = 0$ curve at higher energies. The dashed blue curve for $\mu/\Gamma = 5$ has only a small dip and has recovered to its $\mu = 0$ value by $\Omega/\Gamma = 20$,

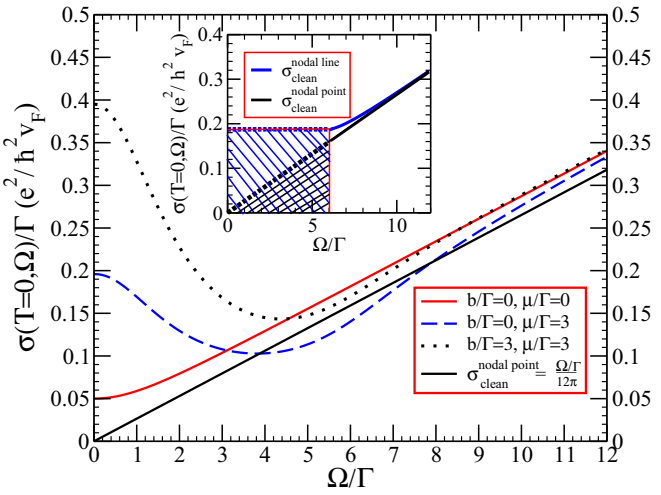

FIG. 7. The optical conductivity $\sigma(T=0,\Omega)$ normalized by the scattering rate Γ in units of $\frac{e^2}{\hbar^2 v_F}$ as a function of normalized photon energy Ω/Γ. The case of $\mu/\Gamma = b/\Gamma = 3$ (dotted black curve) is compared with the case $\mu/\Gamma = 3$ but $b/\Gamma = 0$ (dashed blue curve). Also shown as a solid red line is the case $\mu = b = 0$ and solid black the clean limit. The inset shows results for the clean limit for $\mu = b$ in loop nodes (solid blue) and point node (solid black). The shaded region below $\Omega = 2b$ is entirely transferred to the intraband transition. The ratio of the optical spectral weight transferred of loop and point node $\frac{\mathrm{OSW_{loop}}}{\mathrm{OSW_{point}}}$ is equal to $\frac{3\pi}{4}$.

which is twice the value of 2μ, the low energy cutoff on interband transition that would apply to the clean limit. Here this cutoff is no longer sharp because of the smearing caused by disorder (finite Γ). When the chemical potential is increased to $\mu/\Gamma = 20$ (double-dashed-dotted magenta curve) the conductivity displays a much more pronounced dip beyond the Drude region of photon energy. In the clean limit we would have had a large delta function contribution at $\Omega = 0$ then a complete zero up to $2\mu/\Gamma = 40$ after which it would have recovered its plateau value. Disorder smearing has partially filled in the gap region and has also smeared the edge at 2μ. At still higher values of μ the same behavior is observed but at large Ω/Γ the conductivity goes back to the linear law of 3D point node Dirac.

One interesting special case with some additional commentary is the case $\mu = b$. In the clean limit this corresponds to the transfer of the entire optical spectral weight from the flat 2D graphene-like plateau in the interband conductivity to the intraband delta function at $\Omega = 0$. This leave a region above $\Omega = 2b$ which would deviate very little from the straight line of slope $\frac{1}{12\pi}$ of 3D point node Dirac. Nevertheless the two cases can be differentiated from each other when $\Gamma \neq 0$ as is shown in Fig. 7. The black dotted line is the result for $b/\Gamma = 3$ with $\mu/\Gamma = 3$ as well. We see that the disorder smearing has broadened the intraband transition contribution to such an extent that no Pauli blocking gap is seen at $2\mu/\Gamma = 6$. This is also true for the dashed blue curve obtained when b is set to zero. This curve does differ from the black dotted curve when Γ is included. The main reason for this is that the optical spectral weight under the Drude is very different in the two cases as is illustrated in the inset of the figure. The shaded region shows the lost optical spectral weight (OSW) in the interband background that has been transferred to the intraband. In the clean limit we have $\mathrm{OSW}_{\mathrm{loop}} = \frac{e^2}{\hbar^2 v_F}\frac{b^2}{8}$ for the nodal loop and $\mathrm{OSW}_{\mathrm{point}} = \frac{e^2}{\hbar^2 v_F}\frac{b^2}{6\pi}$ for the 3D point node Dirac. The ratio of the loop to point node is $\frac{3\pi}{4}$. Thus there is more than a factor of 2 difference between these two quantities and this leads to the striking differences between dotted black and dashed blue curves of the main frame of Fig. 7 in the region of photon energy below twice the value of the chemical potential. Above $\Omega/\Gamma \approxeq 10$ both curves are the same and are not very different from the solid red curve for $b = 0$ (3D point node Dirac) including finite Γ and from the solid black curve which is the clean limit version of the solid red curve included for comparison.

IV. DC TRANSPORT

The DC limit of Eq. (3) gives

$$\sigma_{zz}^{\mathrm{IB}}(\Omega=0) = \frac{2e^2\pi}{\hbar^2 v_F}\int_{-\infty}^{+\infty} d\omega\left(-\frac{\partial f(\omega)}{\partial\omega}\right)\sum_{s'}\int\frac{d^3\mathbf{k}}{(2\pi)^3}\left(1-\frac{k_x^2}{\epsilon_{s'}^2(\mathbf{k})}\right)\frac{\Gamma^2}{\pi^2}\left(\frac{1}{\Gamma^2+(\omega-\epsilon_{s'})^2}\times\frac{1}{\Gamma^2+(\omega+\epsilon_{s'})^2}\right) \quad (15)$$

for the interband contribution and

$$\sigma_{zz}^{D}(\Omega=0) = \frac{e^2\pi}{\hbar^2 v_F}\int_{-\infty}^{+\infty} d\omega\left(-\frac{\partial f(\omega)}{\partial\omega}\right)\sum_{s'}\int\frac{d^3\mathbf{k}}{(2\pi)^3}\frac{k_x^2}{\epsilon_{s'}^2(\mathbf{k})}\frac{\Gamma^2}{\pi^2}\left[\left(\frac{1}{\Gamma^2+(\omega-\epsilon_{s'})^2}\right)^2+\left(\frac{1}{\Gamma^2+(\omega+\epsilon_{s'})^2}\right)^2\right] \quad (16)$$

for the intraband or Drude contribution. At zero temperature the thermal factor $-\frac{\partial f(\omega)}{\partial\omega}$ reduces to a delta function of the form $\delta(\omega-\mu)$ which pins ω to be at the chemical potential. Equations (15) and (16) then reduce to 2D integrals over k_x and ρ which are the integration variables introduced in Eq. (8). We get

$$\sigma_{zz}^{\mathrm{IB}}(\Omega=0) = \frac{2e^2\pi}{\hbar^2 v_F}\sum_{s'}\int_0^{+\infty}\frac{\rho d\rho}{(2\pi)^2}\int_{-\infty}^{+\infty} dk_x\frac{\Gamma^2}{\pi^2}\left(1-\frac{k_x^2}{\epsilon_{s'}^2(\mathbf{k})}\right)\left(\frac{1}{\Gamma^2+(\mu-\epsilon_{s'})^2}\times\frac{1}{\Gamma^2+(\mu+\epsilon_{s'})^2}\right), \quad (17)$$

and

$$\sigma_{zz}^{D}(\Omega=0) = \frac{2e^2\pi}{\hbar^2 v_F}\sum_{s'}\int_0^{+\infty}\frac{\rho d\rho}{(2\pi)^2}\int_{-\infty}^{+\infty} dk_x\frac{\Gamma^2}{\pi^2}\frac{k_x^2}{\epsilon_{s'}^2(\mathbf{k})}\left[\left(\frac{1}{\Gamma^2+(\mu-\epsilon_{s'})^2}\right)^2+\left(\frac{1}{\Gamma^2+(\mu+\epsilon_{s'})^2}\right)^2\right]. \quad (18)$$

Results for $\sigma^{\mathrm{DC}}(T=0,\mu) \equiv \sigma_{zz}^{\mathrm{IB}}(\Omega=0)+\sigma_{zz}^{D}(\Omega=0)$ are given in Fig. 8 where we plot $\sigma^{\mathrm{DC}}/\Gamma$ in units of $\frac{e^2}{\hbar^2 v_F}$ as a function of μ/Γ for various values of b/Γ namely $b/\Gamma = 0$ solid black curve, $b/\Gamma = 10$ dashed-dotted blue, $b/\Gamma = 20$ double-dotted-dashed brown, and $b/\Gamma = 30$ dashed green. The solid black line is known from the 3D point node case [16] and is

$$\frac{\sigma^{\mathrm{DC}}(T=0,\mu)}{\Gamma} = \frac{e^2}{\hbar^2 v_F}\frac{1}{2\pi^2}\left[1+\frac{1}{3}\frac{\mu^2}{\Gamma^2}\right]. \quad (19)$$

The limit of zero chemical potential gives

$$\frac{\sigma^{\mathrm{DC}}(T=0,\mu=0)}{\Gamma} = \frac{e^2}{\hbar^2 v_F}\left[\frac{\sqrt{\Gamma^2+b^2}}{2\pi^2\Gamma}\right]. \quad (20)$$

In this case the sum of Eqs. (17) and (18) is particularly simple and the terms $(1-\frac{k_x^2}{\epsilon_{s'}^2(\mathbf{k})})$ in Eq. (17) and $\frac{k_x^2}{\epsilon_{s'}^2(\mathbf{k})}$ in Eq. (18) add to give 1. We get

$$\sigma^{\mathrm{DC}}(T=0,\mu=0) = \frac{2e^2\pi}{\hbar^2 v_F}\sum_{s'}\int_0^{\infty}\frac{\rho d\rho}{(2\pi)^2}\int_0^{\infty} dk_x\frac{\Gamma^2}{\pi^2}\frac{1}{\left(\Gamma^2+\epsilon_{s'}^2\right)^2}, \quad (21)$$

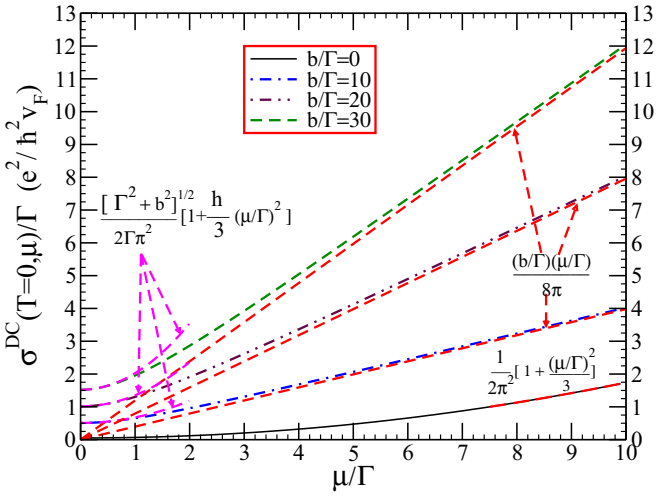

FIG. 8. The DC conductivity $\sigma^{DC}(T=0,\mu)$ normalized by the scattering rate Γ in units of $\frac{e^2}{\hbar^2 v_F}$ as a function of chemical potential μ/Γ for various values of b/Γ. The solid black curve for $b/\Gamma=0$ represents the case of 3D Dirac while all others are for the nodal loop case. In all these cases the asymptotic value at small μ and large μ are indicated by dashed magenta and red lines, respectively. At small μ/Γ a quadratic in μ law holds while at large μ/Γ we have the linear in μ dependence found in Ref. [34] which treated the clean limit. In the present context this limit means both μ/Γ and b/Γ are large.

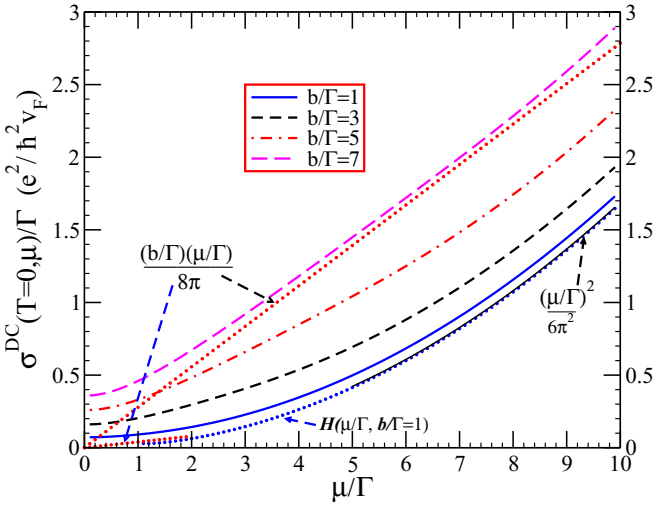

FIG. 9. The DC conductivity $\sigma^{DC}(T=0,\mu)$ normalized by the scattering rate Γ in units of $\frac{e^2}{\hbar^2 v_F}$ as a function of normalized chemical potential μ/Γ for four values of b/Γ namely $b/\Gamma=1$ (solid blue), $b/\Gamma=3$ (dashed black), $b/\Gamma=5$ (dot dashed red), and $b/\Gamma=7$ (dashed magenta). The dotted blue curve shows results in the clean limit for $b/\Gamma=1$ which is described by $\mathcal{H}(\mu/\Gamma,b/\Gamma)$ defined in Eq. (24). The solid black curve shows the quadratic in μ/Γ behavior and matches with the blue dotted curve for values of $\mu/\Gamma > b/\Gamma$. The dotted red curve is for $b/\Gamma=7$ but only the linear part of $\mathcal{H}(\mu/\Gamma,b/\Gamma)$ is shown. Deviations of the dashed magenta curve from this linear law at small values of μ/Γ are due to a finite scattering rate while at large μ/Γ we start seeing deviations due to the evolution of $\mathcal{H}(\mu/\Gamma,b/\Gamma)$ from linear in μ/Γ (2D graphene-like regime) to a quadratic law (3D Dirac point node regime).

which can be done analytically and gives Eq. (20). The implications of Eq. (20) were discussed in the previous section. Here we note that except for the $b/\Gamma=0$ curve $\sigma^{DC}(\mu=0)$ increases linearly with b in Fig. 8 because $b/\Gamma \gg 1$. We shall also show below that for finite μ but $\mu/\Gamma<1$, $\sigma^{DC}(\mu)$ increases as μ^2/Γ^2 out of its $\mu=0$ value. This behavior is indicated by a dashed magenta curve which agrees with our full numerical results at small μ but deviation occurs as μ increases. In fact, for the finite b curves there is a gradual evolution to a linear in μ dependence of $\sigma^{DC}(\mu)$ which is characteristic of 2D graphene-like behavior as obtained in Ref. [34] for the clean limit. Here the clean limit corresponds to μ/Γ and b/Γ large ($\Gamma\to 0$). For $\mu<b$, the clean limit result is

$$\frac{\sigma^{DC}(T=0,\mu)}{\Gamma}=\frac{e^2}{\hbar^2 v_F}\frac{(b/\Gamma)(\mu/\Gamma)}{8\pi}, \tag{22}$$

which is shown in Fig. 8 as the dashed red lines that go through the origin. The main difference between clean limit results and those that included carrier scattering are at small values of μ/Γ (near charge neutrality). Including a finite Γ changes the dependence of the DC conductivity from linear in μ/Γ to a quadratic dependence in the region $\mu/\Gamma<1$. By contrast the solid black curve for $b=0$ follows a quadratic law μ^2/Γ^2 over the entire range shown. The evolution from quadratic to linear behavior is studied in more detail in Fig. 9 where small values of b are considered namely $b=1$ (solid blue), $b=3$ (dashed black), $b=5$ (dashed-dotted red), and $b=7$ (dashed magenta) curves. Also shown on the figure for comparison are clean limit results (dotted blue) for $b=1$ and (dotted red) for $b=7$. What is plotted for the dotted blue line are the results for the clean limit from Ref. [34] (again corrected for a missed factor of 2). The relevant function is

$$\frac{\sigma^{DC}(T=0,\mu)}{\Gamma}=\frac{e^2}{\hbar^2 v_F}\mathcal{H}\left(\frac{\mu}{\Gamma},\frac{b}{\Gamma}\right), \tag{23}$$

with

$$\begin{aligned}\mathcal{H}&\left(\frac{\mu}{\Gamma},\frac{b}{\Gamma}\right)\\ &=\frac{(\mu/\Gamma)(b/\Gamma)}{8\pi}\quad \mu<b,\\ &=\frac{1}{2\pi^2}\left[\frac{1}{2}\left(\frac{\mu}{\Gamma}\right)\left(\frac{b}{\Gamma}\right)\arctan\left(\frac{b/\Gamma}{\sqrt{(\mu/\Gamma)^2-(b/\Gamma)^2}}\right)\right.\\ &\quad\left.+\frac{1}{3}\left(\frac{(\mu/\Gamma)^2-\frac{3}{2}(b/\Gamma)^2}{\mu/\Gamma}\right)\sqrt{(\mu/\Gamma)^2-(b/\Gamma)^2}\right]\mu>b.\end{aligned} \tag{24}$$

For $\mu\gg b$, $\mathcal{H}(\frac{\mu}{\Gamma},\frac{b}{\Gamma})$ of Eq. (24) reduces to $\frac{(\mu/\Gamma)^2}{6\pi^2}$ which is independent of b and the result for 3D point node Dirac. It is clear that there are three regimes for $\mathcal{H}(\frac{\mu}{\Gamma},\frac{b}{\Gamma})$. A linear regime for $\mu<b$, a transition regime for $\mu>b$ during which $\mathcal{H}(\frac{\mu}{\Gamma},\frac{b}{\Gamma})$ evolves from a linear to quadratic dependence on $\frac{\mu}{\Gamma}$, and a final regime where the quadratic law μ^2/Γ^2 holds. The size of μ relative to b is critical in determining which regime is relevant for a particular value of μ. Note that in Fig. 8 the three curves with finite b all fall in the regime $\mu<b$ and so only the linear region of $\mathcal{H}(\frac{\mu}{\Gamma},\frac{b}{\Gamma})$ is probed. In Fig. 9 however we have chosen

b such that the dotted blue curve (clean limit) ranges over all three regimes involved in $\mathcal{H}(\frac{\mu}{\Gamma},\frac{b}{\Gamma})$ as μ/Γ ranges from 0 to 10. Below $\mu/\Gamma = 1$ we are in the linear regime (dotted red curve) and above 8 in the quadratic regime (solid black curve) with a transition region from linear to quadratic between these two extremes. For the dashed magenta curve however we do not show $\mathcal{H}(\frac{\mu}{\Gamma},\frac{b}{\Gamma})$ but rather have chosen to show only the linear dependence even outside its range of validity. It is clear that significant deviations from linearity for large values of μ/Γ enter only for $\mu/\Gamma \geqslant 8$. Comparing the case of finite Γ with its clean limit (dotted curves) we see that the largest effect of finite Γ is in the region $\mu/\Gamma \leqslant 2$ where carrier scattering changes the linear law to a quadratic law.

We now turn to the small μ limit of $\sigma^{\rm DC}(\mu)$ and obtain analytically the μ^2 law seen in Fig. 8. In fact it is convenient to return to Eqs. (17) and (18) and include at the same time finite temperature effects. We take μ/Γ and $T/\Gamma < 1$ in which case it is justified to expand the integrand of Eqs. (17) and (18) to second order in ω dropping all higher order terms. After straightforward algebra we get that the DC conductivity takes the form

$$\sigma^{\rm DC}(\mu,T) = \frac{e^2}{\hbar^2 v_F}\left(\frac{\Gamma^2}{\pi^3}\right)\left[A + B\left(\mu^2 + \frac{\pi^2 T^2}{3}\right)\right], \quad (25)$$

where

$$A = \sum_{s'}\int_0^\infty \rho d\rho \int_0^\infty dk_x \left(\frac{1}{\Gamma^2 + k_x^2 + (\rho + s'b)^2}\right)^2, \quad (26)$$

and $B = B^{\rm IB} + B^D$ with

$$B^{\rm IB} = \sum_{s'}\int_0^\infty \rho d\rho \int_0^\infty dk_x \left(1 - \frac{k_x^2}{k_x^2 + (\rho + s'b)^2}\right)\left[\frac{1}{\left(\Gamma^2 + k_x^2 + (\rho + s'b)^2\right)^3} - \frac{2\Gamma^2}{\left(\Gamma^2 + k_x^2 + (\rho + s'b)^2\right)^4}\right] \quad (27)$$

and

$$B^D = \sum_{s'}\int_0^\infty \rho d\rho \int_0^\infty dk_x \left(\frac{k_x^2}{k_x^2 + (\rho + s'b)^2}\right)\left[\frac{5}{\left(\Gamma^2 + k_x^2 + (\rho + s'b)^2\right)^3} - \frac{6\Gamma^2}{\left(\Gamma^2 + k_x^2 + (\rho + s'b)^2\right)^4}\right]. \quad (28)$$

These integrals can all be done analytically to yield

$$\sigma^{\rm DC}(\mu,T) = \frac{e^2}{2\pi^2\hbar^2 v_F}\left[\sqrt{\Gamma^2 + b^2} + \frac{1}{3\Gamma^2}\left\{\sqrt{\Gamma^2 + b^2} - \frac{\Gamma^2 b^2}{2(\Gamma^2 + b^2)^{3/2}}\right\} \times \left\{\mu^2 + \frac{\pi^2 T^2}{3}\right\}\right]. \quad (29)$$

The limit of $b = 0$ corresponds to 3D point node Dirac. The DC conductivity reduces to

$$\sigma^{\rm DC}(\mu,T) = \frac{e^2\Gamma}{2\pi^2\hbar^2 v_F}\left[1 + \frac{1}{3}\left\{\frac{\mu^2}{\Gamma^2} + \frac{\pi^2}{3}\frac{T^2}{\Gamma^2}\right\}\right], \quad (30)$$

which is a function of μ/Γ and T/Γ valid for both these variables less than one because of our expansion in ω to second order only. The DC conductivity is further linearly proportional to Γ. Expression (30) agrees with the previous work [16] in this limit. For a general b and Γ we get

$$\sigma^{\rm DC}(\mu,T) = \frac{e^2\sqrt{\Gamma^2 + b^2}}{2\pi^2\hbar^2 v_F}\left[1 + \frac{h}{3}\left\{\frac{\mu^2}{\Gamma^2} + \frac{\pi^2}{3}\frac{T^2}{\Gamma^2}\right\}\right], \quad (31)$$

with

$$h = 1 - \frac{\Gamma^2 b^2}{2(\Gamma^2 + b^2)^2}, \quad (32)$$

which is always near 1 in value. Its minimum is at $b = \Gamma$ where it is $\frac{7}{8}$, reduced from one by ~12%. While the $\mu = T = 0$ value of $\sigma^{\rm DC}$ is very different in the nodal loop case from the 3D Dirac point node case, the first going like b while the second goes like Γ, it has the same μ/Γ and T/Γ dependence. T coefficient of this dependence is however always close to that of the point node Dirac.

Other important transport coefficients can also be calculated for $\frac{\mu}{\Gamma},\frac{T}{\Gamma} < 1$. The formula for the conductivity is

$$\sigma^{\rm tot} = \frac{e^2}{\hbar^2 v_F}\frac{\Gamma^2}{\pi^3}\int_{-\infty}^{+\infty} d\omega\left(-\frac{\partial f}{\partial \omega}\right)[A + B\omega^2]. \quad (33)$$

To get thermal conductivity (κ) we drop the e^2 and add a factor of $(\frac{\omega-\mu}{T})^2$ which gives $\frac{\kappa_{22}}{T}$. The total thermal conductivity has a thermopower correction and reads,

$$\frac{\kappa}{T} = \frac{\kappa_{22}}{T} - \frac{e^2\kappa_{12}^2}{\sigma^{\rm DC}}, \quad (34)$$

where the formula for the coefficient κ_{12} is given as in Eq. (33) without the e^2 and a factor $(\frac{\omega-\mu}{T})$ added to the integral of the energy integration over ω. In terms of κ_{12} the thermopower S is given by,

$$S = \frac{e\kappa_{12}}{\sigma^{\rm DC}}. \quad (35)$$

Another quantity often discussed is the Lorentz number (L) of the Wiedemann-Franz law. By definition,

$$L = \frac{\kappa}{T\sigma^{\rm DC}}. \quad (36)$$

It is straightforward to obtain explicit results for the above coefficients using algebra closely related to that of Appendix B of Ref. [16]. The results are,

$$\frac{\kappa_{22}}{T} = \frac{\sqrt{\Gamma^2 + b^2}}{2\pi^2\hbar^2 v_F}\left[1 + h\left\{\frac{1}{9}\frac{\mu^2}{\Gamma^2} + \frac{7\pi^2}{45}\frac{T^2}{\Gamma^2}\right\}\right], \quad (37)$$

$$S = \frac{2\pi^2}{9e}\frac{h(\mu/\Gamma)(T/\Gamma)}{1 + h\left\{\frac{1}{3}\frac{\mu^2}{\Gamma^2} + \frac{\pi^2}{9}\frac{T^2}{\Gamma^2}\right\}}, \quad (38)$$

$$L = \frac{\pi^2}{3e^2}\left[\frac{1 + h\left\{\frac{1}{3}\frac{\mu^2}{\Gamma^2} + \frac{7\pi^2}{15}\frac{T^2}{\Gamma^2}\right\}}{1 + h\left\{\frac{1}{3}\frac{\mu^2}{\Gamma^2} + \frac{\pi^2}{9}\frac{T^2}{\Gamma^2}\right\}}\right], \quad (39)$$

with a correction to L for thermopower of the form S^2. As we have seen $h = 1$ for the point node Dirac case. For the nodal loop case h is somewhat reduced going like $(1 - \frac{1}{2}\frac{\Gamma^2}{b^2})$ for $\Gamma/b < 1$. When the disorder scattering rate becomes large as compared with b we find that h is reduced by 12% at $\Gamma = b$ after which it again rises towards one. These results are only valid for μ/Γ and $T/\Gamma < 1$ near charge neutrality.

The approach to the minimum DC conductivity for $T = \mu = 0$ but with finite Ω as $\Omega \to 0$ is also of interest. It takes on the form of Eq. (31) with the second term in the square bracket replaced by $\frac{1}{36(1+\frac{b^2}{\Gamma^2})^2}[4\frac{b^4}{\Gamma^4} + 6\frac{b^2}{\Gamma^2} + 7]$. The expansion of the functions $\mathfrak{Y}(\widetilde{\mu},\widetilde{\Omega},\widetilde{b},\widetilde{\epsilon}_{s'})$ of Eq. (9) and $\mathfrak{H}(\widetilde{\mu},\widetilde{\Omega},\widetilde{b},\widetilde{\epsilon}_{s'})$ of Eq. (11) in powers of $\widetilde{\Omega}$ and retaining terms to $\widetilde{\Omega}^2$ only gives

$$\frac{\sigma(T=0,\widetilde{\Omega})}{\Gamma} = \frac{e^2}{\hbar^2 v_F}\frac{\sqrt{\Gamma^2+b^2}}{2\pi^2} \times\left[1+\frac{1}{36\left(1+\frac{b^2}{\Gamma^2}\right)^2}\left(4\frac{b^4}{\Gamma^4}+6\frac{b^2}{\Gamma^2}+7\right)\frac{\Omega^2}{\Gamma^2}\right], \quad (40)$$

where we needed to evaluate the integral

$$\frac{e^2}{2\pi^3\hbar^2 v_F}\sum_{s'}\int_0^\infty d\widetilde{k}_x\int_0^\infty \widetilde{\rho}d\widetilde{\rho}\frac{4\widetilde{\epsilon}_{s'}^2 - 2\widetilde{k}_x^2 - 1}{\left(1+\widetilde{\epsilon}_{s'}^2\right)^4} = \frac{4\frac{b^4}{\Gamma^4}+6\frac{b^2}{\Gamma^2}+7}{72\pi^2\left(1+\frac{b^2}{\Gamma^2}\right)^{\frac{3}{2}}}. \quad (41)$$

V. CONCLUSION

We have considered the effect of a finite scattering rate (Γ) on the finite frequency (Ω) electromagnetic response of a nodal loop semimetal and on its DC electrical conductivity, thermal conductivity, thermopower(or Seebeck coefficient), and Lorentz number (or Wiedemann Franz law). For the dynamic optical conductivity at zero temperature $\sigma(T = 0,\Omega)$ several regimes arise as a function of Ω even when the chemical potential is set equal to zero. In the limit of $\Omega \to 0$ which corresponds to the minimum DC (σ^{DC}) conductivity we find $\sigma^{DC} = \frac{e^2\sqrt{\Gamma^2+b^2}}{2\pi^2\hbar^2 v_F}$ where b is the radius of the nodal ring in energy units, e is the electron charge, $\hbar$ the Plank's constant, and v_F the Fermi velocity. This reduces to the known result for 3D point node Dirac when $b = 0$ and to the clean limit result for a nodal semimetal when $\Gamma = 0$. In this last instance the correction for finite Γ is of the order of Γ^2/b^2. The approach to the minimum D.C. conductivity obeys a Ω^2/Γ^2 law with coefficient $\frac{4\frac{b^4}{\Gamma^4}+6\frac{b^2}{\Gamma^2}+7}{36\pi^2(1+\frac{b^2}{\Gamma^2})^2}$. This result agrees with the point node Dirac case of Ref. [16] when $b = 0$. At frequencies a few times Γ but smaller than $2b$ we find a constant interband background as in graphene of height $\frac{e^2}{\hbar^2 v_F}\frac{b}{16}$ provided $b \gg \Gamma$ so that the ratio of $\frac{\sigma^{DC}}{\sigma^{BG}} = \frac{8}{\pi^2}$ and is exactly the same as one would get for graphene in the same constant Γ approximation as used here. Of course both σ^{DC} and σ^{BG} are themselves different in that they both involve material parameters namely v_F and b while in graphene these drop out entirely of both properties. In the limit of $b \to 0$ the constant background loses its integrity and the conductivity $\sigma(T = 0,\Omega)$ evolves toward its behavior in 3D Dirac point node semimetal. For $\Omega > 2b$, $\sigma(T = 0,\Omega)$ again takes on the characteristic linear in Ω dependence and in fact the parameter b completely drops out.

For finite value of the chemical potential μ a Drude-like response is obtained in the regime $\Omega \leqslant 2\mu$ with width related to the scattering rate Γ. In the pure case ($\Gamma = 0$) the region up to $\Omega = 2\mu$ would have zero conductivity but now this region shows only a depressed conductivity because of the disorder scattering. Beyond $\Omega \simeq 2\mu$ the flat background of the $\mu = 0$ case is recovered if $\mu < b$ while we recover the linear dependence of the 3D point node Dirac case if $\mu > b$ with some smearing in the transition region around $\Omega = 2\mu$. Finite chemical potential also affects the behavior of DC properties. For the electrical conductivity we find that provided μ/Γ (or temperature T/Γ) is less than 1 the approach to charge neutrality is quadratic in $\mu/\Gamma(T/\Gamma)$. We have also considered the limit of large μ at $T = 0$ and find the quadratic behavior characteristic of the dirty limit μ^2/Γ^2 approach to charge neutrality and then gradually goes into a linear law μ/Γ characteristic of a 2D graphene-like system when b is much larger than μ and this changes to a μ^2/Γ^2 law for $\mu \gg b$.

Finally the DC thermal conductivity is found to vary as $\frac{\sqrt{\Gamma^2+b^2}}{v_F}$ when $\mu = 0$, $T = 0$ and have a μ^2/Γ^2 or T^2/Γ^2 correction for μ/Γ, T/Γ finite but smaller than one. The coefficient of these quadratic dependences are only slightly modified from the $b = 0$ point node case. The maximum correction for finite b is of order 12%. This implies that the Wiedemann-Franz law only very slightly changes from its value for $b = 0$ (point node case). A similar situation holds for the thermopower. We hope that our calculations will stimulate experimental studies of the optical and transport properties of nodal loop semimetals. In particular AC spectroscopic data can provide a wealth of valuable information on the dynamics of the charge carrier. Several such studies already exist for related systems of Dirac and Weyl semimetals [9–12,14].

ACKNOWLEDGMENTS

Work supported in part by the Natural Sciences and Engineering Research Council of Canada (NSERC) and by the Canadian Institute for Advanced Research (CIFAR).

[1] J. P. Carbotte, T. Timusk, and J. Hwang, Bosons in high-temperature superconductors: an experimental survey, Rep. Prog. Phys. **74**, 066501 (2011).

[2] D. N. Basov and T. Timusk, Electrodynamics of high-T_c superconductors, Rev. Mod. Phys. **77**, 721 (2005).

[3] J. P. Carbotte, C. Jiang, D. N. Basov, and T. Timusk, Evidence for d-wave superconductivity in $YBa_2Cu_3O_7$ from far-infrared conductivity, Phys. Rev. B **51**, 11798 (1995).

[4] Z. Q. Li, E. A. Henriksen, Z. Jiang, Z. Hao, M. C. Martin, P. Kim, H. L. Stormer, and D. N. Basov, Dirac charge dynamics in graphene by infrared spectroscopy, Nat. Phys. **4**, 532 (2008).

[5] L. Stille, C. J. Tabert, and E. J. Nicol, Optical signatures of the tunable band gap and valley-spin coupling in silicene, Phys. Rev. B **86**, 195405 (2012).

[6] J. P. Carbotte, E. J. Nicol, and S. G. Sharapov, Effect of electron-phonon interaction on spectroscopies in graphene, Phys. Rev. B **81**, 045419 (2010).

[7] A. A. Schafgans, K. W. Post, A. A. Taskin, Y. Ando, X.-L. Qi, B. C. Chapler, and D. N. Basov, Landau level spectroscopy of surface states in the topological insulator $Bi_0.91Sb_0.09$ via magneto-optics, Phys. Rev. B **85**, 195440 (2012).

[8] Z. Li and J. P. Carbotte, Optical spectral weight: Comparison of weak and strong spin-orbit coupling, Phys. Rev. B **91**, 115421 (2015).

[9] R. Y. Chen, S. J. Zhang, J. A. Schneeloch, C. Zhang, Q. Li, G. D. Gu, and N. L. Wang, Optical spectroscopy study of the three-dimensional Dirac semimetal $ZrTe_5$, Phys. Rev. B **92**, 075107 (2015).

[10] A. B. Sushkov, J. B. Hofmann, G. S. Jenkins, J. Ishikawa, S. Nakatsuji, S. D. Sarma, and H. D. Drew, Optical evidence for a Weyl semimetal state in pyrochlore $Eu_2Ir_2O_7$, Phys. Rev. B **92**, 241108(R) (2015).

[11] B. Xu, Y. M. Dai, L. X. Zhao, K. Wang, R. Yang, W. Zhang, J. Y. Liu, H. Xiao, G. F. Chen, A. J. Taylor, D. A. Yarotski, R. P. Prasankumar, and X. G. Qiu, Optical spectroscopy of the Weyl semimetal TaAs, Phys. Rev. B **93**, 121110(R) (2016).

[12] D. Neubauer, J. P. Carbotte, A. A. Nateprov, A. Löhle, M. Dressel, and A. V. Pronin, Interband optical conductivity of the [001]-oriented Dirac semimetal Cd_3As_2, Phys. Rev. B **93**, 121202 (2016).

[13] T. Timusk, J. P. Carbotte, C. C. Homes, D. N. Basov, and S. G. Sharapov, Three-dimensional Dirac fermions in quasicrystals as seen via optical conductivity, Phys. Rev. B **87**, 235121 (2013).

[14] M. Chinotti, A. Pal, W. J. Ren, C. Petrovic, and L. Degiorgi, Electrodynamic response of the type-II Weyl semimetal $YbMnBi_2$, Phys. Rev. B **94**, 245101 (2016).

[15] C. J. Tabert and J. P. Carbotte, Optical conductivity of Weyl semimetals and signatures of the gapped semimetal phase transition, Phys. Rev. B **93**, 085442 (2016).

[16] C. J. Tabert, J. P. Carbotte, and E. J. Nicol, Optical and transport properties in three-dimensional Dirac and Weyl semimetals, Phys. Rev. B **93**, 085426 (2016).

[17] J. P. Carbotte, Dirac cone tilt on interband optical background of type-I and type-II Weyl semimetals, Phys. Rev. B **94**, 165111 (2016).

[18] A. A. Burkov, M. D. Hook, and L. Balents, Topological nodal semimetals, Phys. Rev. B **84**, 235126 (2011).

[19] M. Phillips and V. Aji, Tunable line node semimetals, Phys. Rev. B **90**, 115111 (2014).

[20] J.-M. Carter, V. V. Shankar, M. A. Zeb, and H.-Y. Kee, Semimetal and Topological Insulator in Perovskite Iridates, Phys. Rev. B **85**, 115105 (2012).

[21] Y. Kim, B. J. Wieder, C. L. Kane, and A. M. Rappe, Dirac Line Nodes in Inversion-Symmetric Crystals, Phys. Rev. Lett. **115**, 036806 (2015).

[22] H. Weng, Y. Liang, Q. Xu, R. Yu, Z. Fang, X. Dai, and Y. Kawazoe, Topological node-line semimetal in three-dimensional graphene networks, Phys. Rev. B **92**, 045108 (2015).

[23] K. Mullen, B. Uchoa, and D. T. Glatzhofer, Line of Dirac Nodes in Hyperhoneycomb Lattices, Phys. Rev. Lett. **115**, 026403 (2015); L. S. Xie, L. M. Schoop, E. M. Seibel, Q. D. Gibson, W. Xie, and R. J. Cava, A new form of Ca_3P_2 with a ring of Dirac nodes, APL Mater. **3**, 083602 (2015).

[24] C. Fang, Y. Chen, H.-Y. Kee, and L. Fu, Topological nodal line semimetals with and without spin-orbital coupling, Phys. Rev. B **92**, 081201(R) (2015).

[25] G. Bian, T.-R. Chang, R. Sankar, S.-Y. Xu, H. Zheng, T. Neupert, C.-K. Chiu, S.-M. Huang, G. Chang, I. Belopolski, D. S. Sanchez, M. Neupane, N. Alidoust, C. Liu, B. Wang, C.-C. Lee, H.-T. Jeng, C. Zhang, Z. Yuan, S. Jia, A. Bansil, F. Chou, H. Lin, and M. Z. Hasan, Topological nodal-line fermions in spin-orbit metal $PbTaSe_2$, Nat. Commun. **7**, 10556 (2016).

[26] A. Yamakage, Y. Yamakawa, Y. Tanaka, and Y. Okamoto, Line-Node Dirac Semimetal and Topological Insulating Phase in Noncentrosymmetric Pnictides CaAgX (X = P, As), J. Phys. Soc. Jpn. **85**, 013708 (2016).

[27] L. Li and M. A. N. Arajo, Topological insulating phases from two-dimensional nodal loop semimetals, Phys. Rev. B **94**, 165117 (2016); K.-H. Ahn, K.-W. Lee, and W. E. Pickett, Spin-orbit interaction driven collective electron-hole excitations in a noncentrosymmetric nodal loop Weyl semimetal, *ibid.* **92**, 115149 (2015).

[28] M. Ezawa, Loop-Nodal and Point-Nodal Semimetals in Three-Dimensional Honeycomb Lattices, Phys. Rev. Lett. **116**, 127202 (2016).

[29] M. Koshino and I. F. Hizbullah, Magnetic susceptibility in three-dimensional nodal semimetals, Phys. Rev. B **93**, 045201 (2016).

[30] J.-W. Rhim and Y. B. Kim, Anisotropic density fluctuations, plasmons, and Friedel oscillations in nodal line semimetal, New J. Phys. **18**, 043010 (2016).

[31] J.-W. Rhim and Y. B. Kim, Landau level quantization and almost flat modes in three-dimensional semimetals with nodal ring spectra, Phys. Rev. B **92**, 045126 (2015).

[32] S. T. Ramamurthy and T. L. Hughes, Quasitopological electromagnetic response of line-node semimetals, Phys. Rev. B **95**, 075138 (2017).

[33] J. Liu and L. Balents, Correlation effects and quantum oscillations in topological nodal-loop semimetals, Phys. Rev. B **95**, 075426 (2017).

[34] J. P. Carbotte, Optical response of a line node semimetal, J. Phys.: Condens. Matter. **29**, 045301 (2017).

[35] V. P. Gusynin, S. G. Sharapov, and J. P. Carbotte, On the universal ac optical background in graphene, New J. Phys. **11**, 095013 (2009).

[36] P. A. Lee, Localized States in a *d*-Wave Superconductor, Phys. Rev. Lett. **71**, 1887 (1993).

[37] C. O'Donovan, and J. P. Carbotte, Mixed order parameter symmetry in the BCS model, Physica C **252**, 87 (1995).

[38] C. O'Donovan and J. P. Carbotte, *s*- and *d*-wave mixing in high-T_c superconductors, Phys. Rev. B **52**, 16208 (1995).

[39] M. J. Graf, S.-K. Yip, J. A. Sauls, and D. Rainer, Electronic thermal conductivity and the Wiedemann-Franz law for unconventional superconductors, Phys. Rev. B **53**, 15147 (1996).

[40] I. Schürrer, E. Schachinger, and J. P. Carbotte, Optical conductivity of superconductors with mixed symmetry order parameters, Physica C **303**, 287 (1998).

[41] H. K. Leung, J. P. Carbotte, D. W. Taylor, and C. R. Leavens, Effect of Fermi surface anisotropy on the thermody-

namics of superconducting Al, Canadian J. Phys. **54**, 1585 (1976).

[42] F. Evers and A. D. Mirlin, Anderson transitions, Rev. Mod. Phys. **80**, 1355 (2008).

[43] T. Holder, C.-W. Huang, and P. Ostrovsky, Electronic properties of disordered Weyl semimetals at charge neutrality, arXiv:1704.05481 (2017).

[44] B. Roy, V. Juričić, and S. D. Sarma, Universal optical conductivity of a disordered Weyl semimetal, Scientific Reports, **6**, 32446 (2016).

[45] Y. Ominato and M. Koshino, Quantum transport in a three-dimensional Weyl electron system, Phys. Rev. B **89**, 054202 (2014).